RSC Advances

PAPER

View Article Online
View Journal | View Issue

Check for updates

Cite this: *RSC Adv.*, 2026, **16**, 748

Strain engineering of optoelectronic and ferroelectric properties in *R*3-phase Zn_3TeO_6: a first-principles study

Xing-Yuan Chen, *[a] Guo-Wei Lai,[a] Tu-Rong Ning,[a] Yan-Li Hu,[a] Xiao-Dong Yang,[a] Shuang-Rui Chen,[b] Yin Liu[a] and Hua-Kai Xu*[a]

A systematic evaluation of the optoelectronic properties of ferroelectric ternary oxides under strain is essential for their integration into functional devices. In this study, the *R*3-phase ternary oxide Zn_3TeO_6 was investigated using density functional theory to examine its stability, electronic structure, optical properties, ferroelectric behavior, and carrier mobility under both compressive and tensile strain. Calculations of elastic constants, molecular dynamics simulations, and phonon spectra confirm the stability of Zn_3TeO_6 within a modest strain range. Compressive strain increases phonon frequencies, elastic constants, and bandgap, while enhancing ferroelectric polarization. In contrast, tensile strain decreases the bandgap and promotes visible-light absorption. Carrier transport analysis reveals pronounced n-type conduction, with electron mobility reaching ~150 $cm^2\ V^{-1}\ s^{-1}$, further enhanced under compressive strain due to the suppression of polar optical phonon and piezoelectric scattering. These findings demonstrate that strain engineering offers an effective approach to tuning the multifunctional properties of *R*3-Zn_3TeO_6, highlighting its potential for ferroelectric and photovoltaic applications.

Received 7th November 2025
Accepted 18th December 2025

DOI: 10.1039/d5ra08570e

rsc.li/rsc-advances

Open Access Article. Published on 02 January 2026. Downloaded on 2/10/2026 6:34:07 PM. This article is licensed under a Creative Commons Attribution-NonCommercial 3.0 Unported Licence.

1. Introduction

X_3TeO_6 compounds (where X is a 3d transition metal) have attracted considerable attention due to their unique magnetic, electric, and dielectric properties.[1–5] Their complex magnetic behaviors and field-induced polarization effects, particularly the antiferromagnetic transitions and colossal magnetoelectric coupling observed in several members, highlight their great potential for multifunctional device applications.[1,3,5] Zn_3TeO_6 crystallizes in an isostructural β-Li_3VF_6-type structure, similar to X_3TeO_6, and contains five distinct Zn^{2+} coordination environments, including distorted octahedral, tetrahedral, and square-pyramidal sites.[6–8] While the C2/c phases of Co_3TeO_6 and Zn_3TeO_6 are enthalpically favored below 10 GPa, the *R*3 phase becomes energetically more stable above this pressure, resulting in a $C2/c \rightarrow R3$ structural transition.[9] While the *R*3 phase is a high-pressure phase in bulk materials, substrate-induced strain in epitaxial thin films can plausibly stabilize its polar structure as the energetic ground state, similar to the stabilization of polar *R*3c $MgSnO_3$ films grown epitaxially or by pulsed laser deposition.[10,11] Fernández-Catalá *et al.* successfully synthesized nanoscale Ni_3TeO_6 (*R*3) and Cu_3TeO_6 ($Ia\bar{3}$) *via* an NaOH-assisted hydrothermal method, finding both materials exhibit semiconducting behavior (with respective band gaps of 2.44 eV and 2.56 eV) and pronounced photoconductivity.[12] A high-pressure phase, Mg_3TeO_6 (space group *R*3), was obtained under 12.5 GPa and 1570 K, with an experimental band gap of 3.5 eV, confirming its wide-bandgap semiconducting nature.[13] Furthermore, crystallographic and optical investigations of $Co_{3-x}Zn_xTeO_6$ revealed that Zn dopants preferentially occupy tetrahedral sites, enhancing local distortion, while the strong covalent character of Co–O bonds significantly affect the optical response.[14] Magnetic studies by Sarkar *et al.* demonstrated that Zn substitution shortens the Co^{2+}–O bond length and markedly suppresses the magnetic interactions in Co_3TeO_6.[15] X_3TeO_6 compounds with the *R*3 structure not only have potential applications in magnetism, photoconductivity, and as semiconductors, but this polar *R*3 structure also suggests potential ferroelectric behavior, implying potential ferroelectric photovoltaic properties.[16–18]

By applying tensile strain, the structural stability, bandgap characteristics, and optical responses of various emerging two-dimensional materials (such as Si_2C, C_3B, and h-BC_2N) can be effectively tuned, enabling bandgap modulation and enhanced optical absorption, which highlights the crucial role of strain engineering in optimizing their optoelectronic performance.[19–21] Likewise, for three-dimensional ferroelectric materials, strain engineering has also become an indispensable

[a]*Department of Physics, School of Science, Guangdong University of Petrochemical Technology, Maoming 525000, Guangdong, PR China. E-mail: chenxingyuan@gdupt.edu.cn; xuhuakai@gdupt.edu.cn; Fax: +86-668-2923567; Tel: +86-668-2923838*
[b]*Department of Architectural Engineering, Guangdong University of Petrochemical Technology, PR China*

© 2026 The Author(s). Published by the Royal Society of Chemistry

Open Access Article. Published on 02 January 2026. Downloaded on 2/10/2026 6:34:07 PM.
This article is licensed under a Creative Commons Attribution-NonCommercial 3.0 Unported Licence.

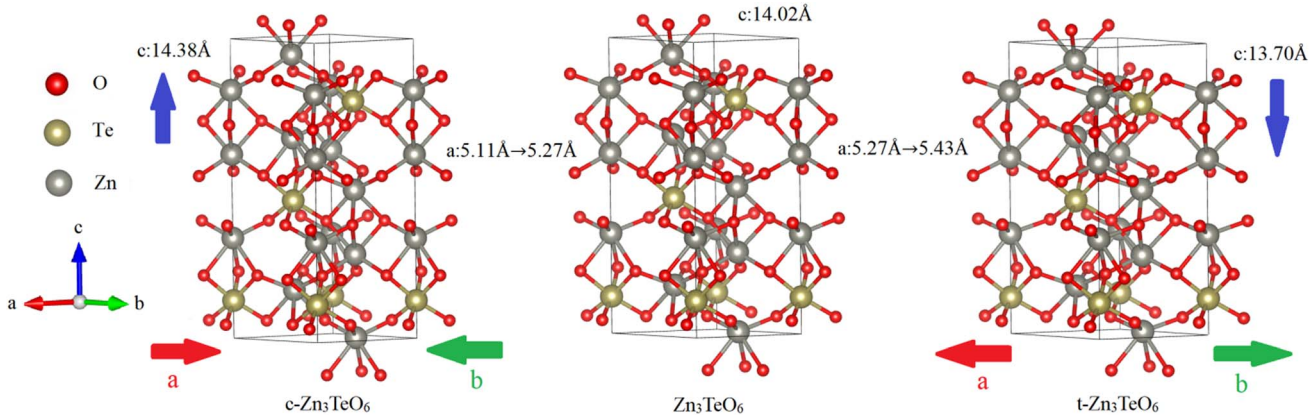

Fig. 1 The structure of *R*3-Zn_3TeO_6.

strategy for tailoring their intrinsic properties. Compared with chemical doping or external fields, strain offers advantages such as reversibility, continuity, and high precision, enabling the modulation of structural stability as well as electronic, magnetic, and optical properties without introducing chemical complexity.[22–24] Epitaxial strain, for instance, can reconstruct band structures, leading to bandgap enlargement and corresponding modifications of the optical response in materials such as *R*3c-$BiFeO_3$.[25] Strain effects during synthesis are also critically important, as research has shown that the lattice strain introduced by reducing the heating rate during calcination can enhance the oxygen evolution reaction (OER) activity and stability of Ni_3TeO_6 electrocatalysts.[26] It is reported in the literature that epitaxial strain can enhance ferroelectric properties while also favorably modifying the optical response of thin films, supporting their viability for optoelectronic device applications.[27]

Despite substantial advances in elucidating the magnetic properties of the X_3TeO_6 system, its optoelectronic behavior—particularly the evolution of electronic structure and carrier dynamics of Zn_3TeO_6 under different strain conditions—remains insufficiently explored. In this work, first-principles calculations combined with strain engineering are employed to investigate the structural stability, band modulation, carrier transport, and polarization response of *R*3-Zn_3TeO_6 under both compressive and tensile strains. The aim is to uncover the mechanisms by which strain regulates its thermodynamic and mechanical stability as well as its coupled optoelectronic–ferroelectric properties, thereby providing theoretical guidance for the design and device integration of multifunctional tellurates.

2. Calculation model and method

All calculations in this work are mainly completed by the Vienna *Ab initio* Simulation Package (VASP) software package for first-principles calculations.[28,29] The interaction between electrons and atomic nuclei in the computational system is described using the projection additive wave (PAW) pseudo potential,[30] and the exchange correlation functional between electrons is processed using the generalized gradient approximation (GGA) of Perdew–Burke–Ernzerhof (PBE).[31] The Heyd–Scuseria–Ernzerhof (HSE06) hybrid functional is used to calculate the bandgap values and optical properties, as it is usually closer to the experimental values.[32,33] A plane-wave cutoff energy of 520 eV was employed, and the Brillouin zone was sampled using a 7 × 7 × 3 gamma-centered *k*-point mesh. The electronic configurations of pseudo potential for Zn, Te, and O atoms are chosen as $d^{10}p^2$, s^2p^4, and s^2p^4, respectively. The iterative convergence accuracy of the energy is set to 10^{-6} eV, and the Hellman–Feynman forces are less than 0.01 eV $Å^{-1}$. The structural model of *R*3-Zn_3TeO_6 is shown in Fig. 1, which contains 30 atoms.

The calculated lattice parameters are shown in Table 1. The calculated lattice parameters a and c of *R*3-Zn_3TeO_6 by PBE method are 5.27 Å and 14.02 Å. As shown in Fig. 1, introducing a 3% compressive strain in the ab plane of *R*3-Zn_3TeO_6 reduces the lattice parameter a from 5.27 Å to 5.11 Å. At the same time, the lattice parameter c of *R*3-Zn_3TeO_6 under compression strain in the ab direction is changed to 14.38 Å, which is larger than the intrinsic *R*3-Zn_3TeO_6. When a similar tensile strain is introduced in the *R*3-Zn_3TeO_6 along ab plane, the lattice parameters a and c of *R*3-Zn_3TeO_6 are changed to 5.43 Å and 13.70 Å, respectively. When the compressive and tensile strains increase to 6%, the variation trends of the lattice parameters *a* and *c* remain essentially consistent with those observed under 3% strain. In all tables and pictures, c-Zn_3TeO_6 and t-Zn_3TeO_6 have been used to express as Zn_3TeO_6 under compressive strain and tensile strain, respectively. The lattice *a*/*c* ratios of Zn_3TeO_6 approach 0.37, closely matching those of Co_3TeO_6,[9] Ni_3TeO_6

Table 1 The calculated lattice parameters by PBE method

*R*3	*a* (Å)	*c* (Å)
c-Zn_3TeO_6 (−6%)	4.96	14.78
c-Zn_3TeO_6 (−3%)	5.11	14.38
Zn_3TeO_6	5.27	14.02
t-Zn_3TeO_6 (3%)	5.43	13.70
t-Zn_3TeO_6 (6%)	5.59	13.45
Co_3TeO_6 (ref. 9)	5.19	13.80
Ni_3TeO_6 (ref. 10)	5.11	13.75
Mg_3TeO_6 (ref. 11)	5.14	13.81

© 2026 The Author(s). Published by the Royal Society of Chemistry

Open Access Article. Published on 02 January 2026. Downloaded on 2/10/2026 6:34:07 PM.
This article is licensed under a Creative Commons Attribution-NonCommercial 3.0 Unported Licence.

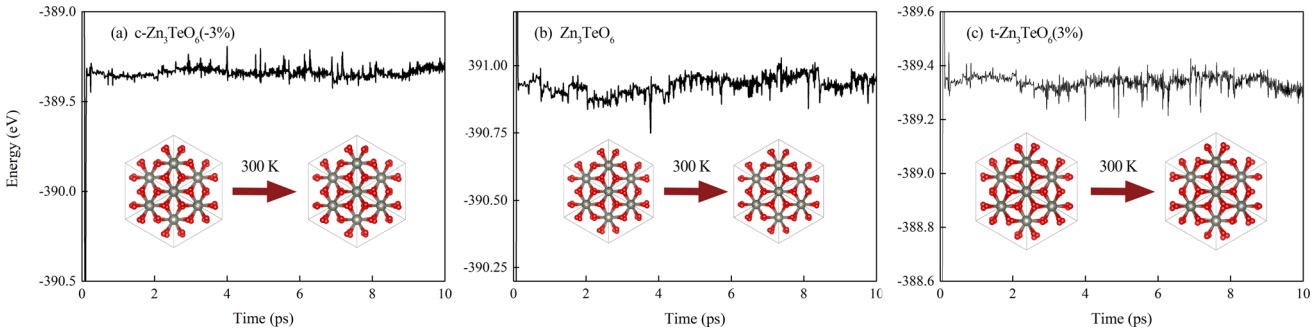

Fig. 2 AIMD energy evolution of Zn_3TeO_6 under (a) −3% compressive strain, (b) the unstrained structure, and (c) +3% tensile strain.

(ref. 12) and Mg_3TeO_6,[13] indicating a highly similar crystal structure. The stability and photoelectric properties of *R*3-Zn_3TeO_6 under compressive and tensile strain have been analyzed by elastic properties, phonon spectrum and electronic structure.

3. Results and discussion

3.1 Stability and mechanical properties

Ab initio molecular dynamics (AIMD) simulations were performed at 300 K within the *NVT* ensemble using the Nosé–Hoover thermostat, with a time step of 2 fs and a total simulation duration of 10 ps. Fig. 2 presents the evolution of the total energy of Zn_3TeO_6 under various strain conditions. As shown in Fig. 2, the compressive (−3%), unstrained, and tensile (+3%) configurations exhibit only minor fluctuations in total energy throughout the simulation, with no abrupt changes or indications of structural collapse. The atomic configurations after the AIMD run remain essentially identical to their initial structures, with no bond breaking or noticeable lattice distortion observed. These results confirm that *R*3-Zn_3TeO_6 retains good thermal and dynamic stability within the investigated strain range. In addition to the ±3% strain discussed in the main text, AIMD simulations under larger biaxial strains of −6% and +6% were included in the SI to provide a more comprehensive assessment of the strain-dependent thermal stability of *R*3-Zn_3TeO_6. As shown in Fig. S1 (SI), the system under −6% compressive strain exhibits an upward trend in total energy during the 300 K, 10 ps simulation, suggesting potential instability despite the absence of structural collapse or bond breaking. In contrast, the +6% tensile configuration shows relatively stable energy fluctuations and remains structurally intact, indicating that it still maintains dynamic stability. Overall, the stability of Zn_3TeO_6 deteriorates under such large strain conditions.

The phonon spectra of *R*3-Zn_3TeO_6 under compressive and tensile strain were calculated using the VASP + PHONOPY package.[34] As displayed in Fig. 3, all phonon frequencies are positive with no imaginary modes, demonstrating that the material satisfies the dynamic stability criteria within this strain range. Furthermore, compressive strain increases phonon frequencies, whereas tensile strain reduces them, indicating that compressive strain enhances the dynamic stability of *R*3-Zn_3TeO_6 while tensile strain slightly weakens it. Phonon calculations under larger biaxial strains of −6% and +6% were also provided in the SI. As shown in Fig. S2 (SI, imaginary phonon modes appear under both strain conditions,

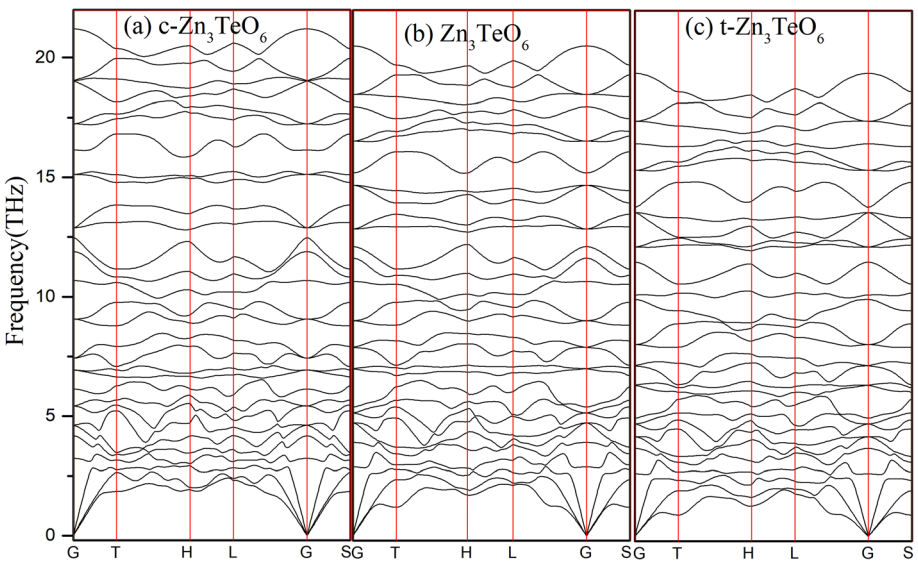

Fig. 3 The calculated phonon frequency of (a) c-Zn_3TeO_6, (b) Zn_3TeO_6 and (c) t-Zn_3TeO_6.

© 2026 The Author(s). Published by the Royal Society of Chemistry

Open Access Article. Published on 02 January 2026. Downloaded on 2/10/2026 6:34:07 PM. This article is licensed under a Creative Commons Attribution-NonCommercial 3.0 Unported Licence.

Table 2 The calculated elastic constants and the unit is given in GPa

*R*3	C_{11}	C_{12}	C_{13}	C_{14}	C_{15}	C_{33}	C_{44}
c-Zn_3TeO_6 (−6%)	290.948	177.480	127.568	14.680	1.569	285.218	32.349
c-Zn_3TeO_6 (−3%)	270.858	151.487	104.092	16.212	2.533	244.507	34.758
Zn_3TeO_6	238.136	130.239	79.997	17.669	8.430	202.499	26.784
t-Zn_3TeO_6 (3%)	207.301	121.390	62.335	19.075	14.730	174.200	19.133
t-Zn_3TeO_6 (6%)	141.795	114.394	34.617	20.679	19.190	139.421	16.947

Table 3 The calculated Bulk modulus *B*, Shear modulus *G* and Young's modulus *E*

*R*3	*B* (GPa)	*G* (GPa)	*E* (GPa)
c-Zn_3TeO_6 (−6%)	192.957	52.858	145.307
c-Zn_3TeO_6 (−3%)	166.064	48.519	132.638
Zn_3TeO_6	138.108	38.794	106.417
t-Zn_3TeO_6 (3%)	117.896	24.267	68.126
t-Zn_3TeO_6 (6%)	93.096	14.764	46.763

confirming that the dynamic stability of Zn_3TeO_6 deteriorates significantly when subjected to such large strains.

To assess the mechanical stability of *R*3-Zn_3TeO_6 under compressive and tensile strain, the elastic constants were calculated using the VASP package, as summarized in Table 2. Owing to the symmetry of the trigonal/rhombohedral system (*R*3 space group), seven independent elastic constants were obtained. According to the stability criteria proposed by Mouhat and Coudert,[35] *R*3-Zn_3TeO_6 is mechanically stable when the following inequalities are satisfied:

$$\text{(i) } C_{11} > |C_{12}|$$

$$\text{(ii) } C_{13}^2 < 0.5 \times C_{33} \times (C_{11} + C_{12})$$

$$\text{(iii) } C_{14}^2 + C_{15}^2 < 0.5C_{44} \times (C_{11} - C_{12})$$

$$\text{(iv) } C_{44} > 0$$

Our results show that under +6% tensile strain, the elastic constants fail to satisfy these inequalities, indicating mechanical instability. In contrast, the unstrained configuration and all other strain states meet the criteria and thus remain mechanically stable. Notably, compressive strain increases the elastic constants, implying enhanced mechanical strength, whereas tensile strain reduces them, leading to weakened stability. This trend is consistent with our previous findings.[36] We further evaluated the bulk modulus *B*, shear modulus *G*, and Young's modulus *E* using the Voigt–Reuss–Hill (VRH) approximation.[37] The explicit formulas are:

$$B_V = \frac{1}{9}[2(C_{11} + C_{12}) + C_{33} + 4C_{13}]$$

$$G_V = \frac{1}{30}(C_{11} + C_{12} + 2C_{33} - 4C_{13} + 12C_{44} + 12C_{66})$$

$$B_R = \frac{(C_{11} + C_{12})C_{33} - 2C_{13}^2}{C_{11} + C_{12} + 2C_{33} - 4C_{13}}$$

$$G_R = \frac{5}{2}\frac{[(C_{11} + C_{12})C_{33} - 2C_{13}^2]C_{44}C_{66}}{3B_VC_{44}C_{66} + [(C_{11} + C_{12})C_{33} - 2C_{13}^2](C_{44} + C_{66})}$$

$$C_{66} = \frac{1}{2}(C_{11} - C_{12})$$

$$B = \frac{1}{2}(B_V + B_R)$$

$$G = \frac{1}{2}(G_V + G_R)$$

$$E = \frac{9BG}{3B + G}$$

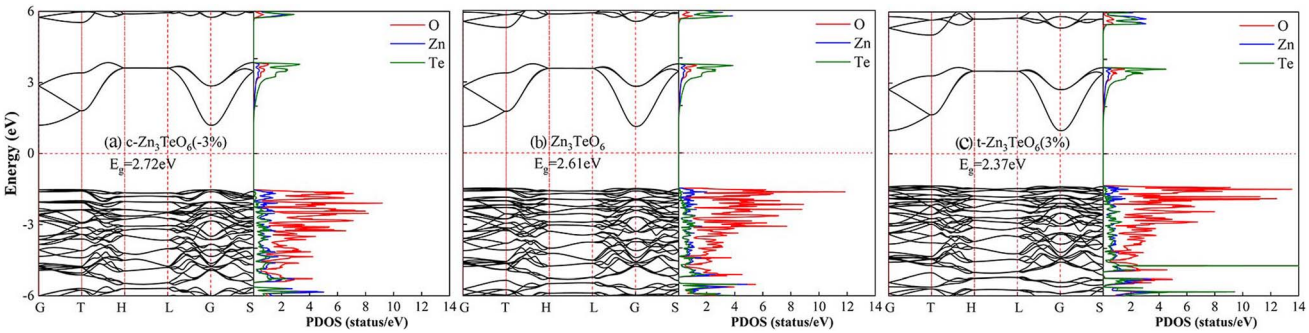

Fig. 4 The calculated band structure and density of states of (a) c-Zn_3TeO_6, (b) Zn_3TeO_6 and (c) t-Zn_3TeO_6.

Open Access Article. Published on 02 January 2026. Downloaded on 2/10/2026 6:34:07 PM. This article is licensed under a Creative Commons Attribution-NonCommercial 3.0 Unported Licence.

Table 4 The calculated bond length of Zn–O and Te–O. The unit is given in Å

	Zn1–O1	Zn1–O2	Zn2–O1	Zn2–O2	Zn3–O1	Zn3–O2	Te–O1	Te–O2
c-Zn_3TeO_6 (−6%)	2.25	2.00	2.00	2.18	1.95	2.18	1.96	1.92
c-Zn_3TeO_6 (−3%)	2.30	2.02	1.99	2.23	2.02	2.23	1.97	1.94
Zn_3TeO_6	2.33	2.04	2.03	2.27	2.05	2.29	1.98	1.95
t-Zn_3TeO_6 (3%)	2.36	2.07	2.08	2.32	2.08	2.35	2.00	1.97
t-Zn_3TeO_6 (6%)	2.37	2.10	2.09	2.45	2.14	2.30	2.01	1.98

As summarized in Table 3, compressive strain leads to an increase in Young's modulus, whereas tensile strain reduces it, consistent with trends reported in previous literature.[36] Integrating the results from molecular dynamics, phonon spectra, and elasticity-based stability analyses, we conclude that *R*3-Zn_3TeO_6 remains stable under small strains (±3%), while larger strains (±6%) are prone to inducing instability. This is in agreement with experimental observations: during the fabrication of three-dimensional polar films *via* pulsed laser deposition (PLD) or molecular beam epitaxy (MBE), substrates with closely matched lattice parameters are typically required.[10,11] Therefore, in the following discussions on electronic structure, band dispersion, optical properties, ferroelectric polarization, and carrier transport behavior, we primarily focus on configurations under small strain (±3%).

3.2 Optoelectronic property

The energy band structure and densities of states (DOS) for *R*3-Zn_3TeO_6 under unstrained, compressive, and tensile conditions were calculated using the HSE06 hybrid functional. As shown in Fig. 4, the unstrained *R*3-Zn_3TeO_6 exhibits a calculated band gap of 2.60 eV. This value modulates under applied strain, widening to 2.72 eV under compressive strain (c-Zn_3TeO_6) and narrowing to 2.36 eV under tensile strain (t-Zn_3TeO_6). These calculated band gaps are considerably smaller than that of HP-Mg_3TeO_6 (3.5 eV), suggesting potential for absorption over a broader portion of the visible spectrum and potentially enhanced photoelectric conversion efficiency.[13] Specifically, the band gap narrowing under tensile strain suggests enhanced visible light absorption, whereas the band gap widening under compression is expected to shift the absorption onset toward the ultraviolet region, reducing responsiveness to visible light. Analysis of the projected densities of states (PDOS) in Fig. 4 indicates that considerable hybridization between O 2p and Zn 3d orbitals occurs within the valence band (*ca.* −3.5 to −2.0 eV). This hybridization likely plays a significant role in determining the material's primary electronic properties. The states near the valence band maximum (VBM) are predominantly composed of hybridized O–Zn orbitals, while the states near the conduction band minimum (CBM) are mainly derived from O–Te hybrid orbitals. For both the VBM and CBM, O 2p states provide the most significant contribution. Compared to the unstrained structure, c-Zn_3TeO_6 exhibits a lower density of O-derived states at the VBM, whereas t-Zn_3TeO_6 shows a higher density. Simultaneously, the CBM energy level shifts upward for c-Zn_3TeO_6 and downward for t-Zn_3TeO_6 relative to the unstrained case. The mechanism for this band gap widening under compression is consistent with the findings of Liu H. L. *et al.*[23] and can be attributed to the shortening of O–Zn and O–Te bond lengths Table 4, which enhances orbital overlap. The band structures of Zn_3TeO_6 under ±6% compressive and tensile strain were also calculated, and the results are provided in the SI (Fig. S3). The bandgaps obtained under 6% compressive and 6% tensile strain are 2.68 eV and 2.03 eV, respectively. Relative to the unstrained state, the compressive strain results in an increased bandgap, whereas the tensile strain leads to a reduced bandgap.

The absorption coefficient $\alpha(\omega)$ can be obtained from the real part $\varepsilon_1(\omega)$ and imaginary part $\varepsilon_2(\omega)$ of the dielectric function *via*

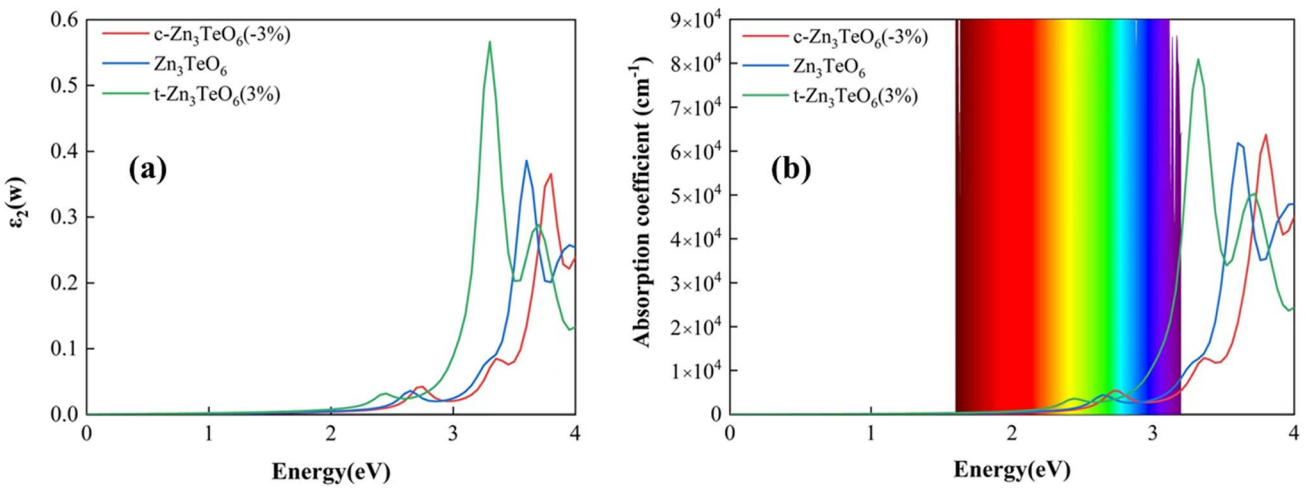

Fig. 5 (a) Imaginary component of the dielectric function (ε_2) and (b) optical absorption coefficient (α) of Zn_3TeO_6.

© 2026 The Author(s). Published by the Royal Society of Chemistry

Open Access Article. Published on 02 January 2026. Downloaded on 2/10/2026 6:34:07 PM.
This article is licensed under a Creative Commons Attribution-NonCommercial 3.0 Unported Licence.

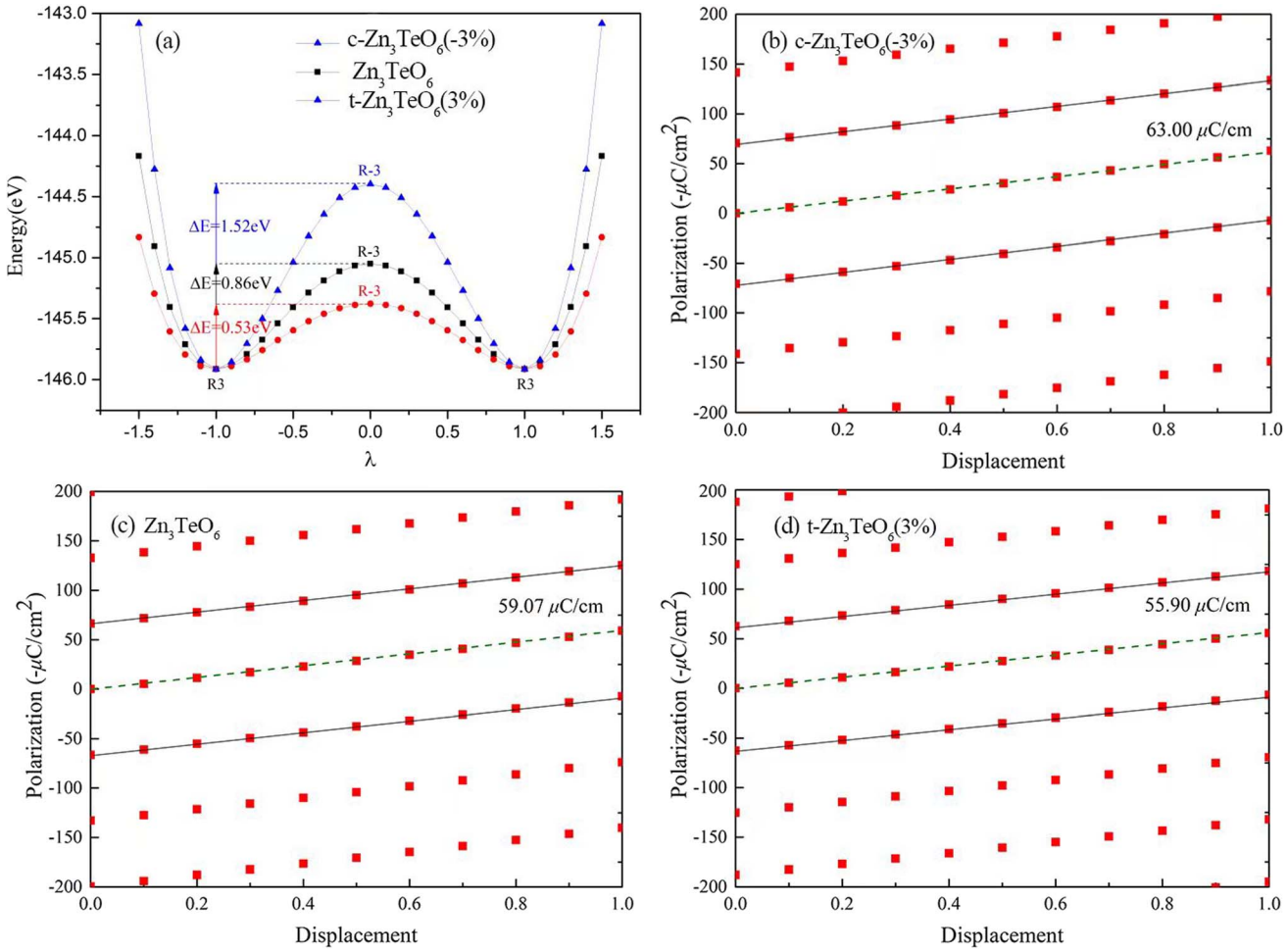

Fig. 6 (a) Potential energy curves and ferroelectric polarization as a function of structural distortion for (b) −3% compressive strain, (c) the unstrained structure, and (d) +3% tensile strain.

the formula $\alpha(\omega) = \frac{\sqrt{2}\omega}{c}\left[\sqrt{\varepsilon_1(\omega)^2 + \varepsilon_2(\omega)^2} - \varepsilon_1(\omega)\right]^{1/2}$. As shown in Fig. 5, pristine Zn_3TeO_6 and its strained counterparts exhibit consistent optical-response trends in both $\varepsilon_2(\omega)$ and $\alpha(\omega)$: negligible absorption is found in the low-energy region (<~2.2 eV), indicating weak intrinsic absorption in the visible range, whereas a sharp rise emerges near the band edge, giving rise to pronounced peaks. Consequently, all three structures show strong ultraviolet absorption above ~3 eV, with maximum absorption coefficients on the order of 10^4 cm^{-1}. A clear divergence appears under tensile *versus* compressive strain. The 3% tensile strain narrows the band gap, causing a red shift of the absorption edge for t-Zn_3TeO_6 to ~2.8 eV and producing a stronger main peak around 3.1–3.3 eV (maximum $\varepsilon_2 \approx 0.55$ with a corresponding absorption peak of ~8 × 10^4 cm^{-1}), thereby enabling enhanced near-UV and lower-energy photon absorption. In contrast, −3% compressive strain widens the band gap, shifting the absorption edge of c-Zn_3TeO_6 to higher energy (~3.1 eV) and slightly moving the main peak toward ~3.7–3.8 eV with reduced intensity, confining its dominant response to the ultraviolet region. These results confirm that strain engineering is an effective approach for tuning band-edge optical transitions and optimizing the electronic and optical properties of *R*3-Zn_3TeO_6.

3.3 Ferroelectric property

The ferroelectric polarization of unstrained, compressively strained, and tensile-strained *R*3-Zn_3TeO_6 was calculated using the Berry-phase method.[38,39] Following this approach, a centrosymmetric *R*3 reference structure was constructed, and the energy and polarization were obtained through linear interpolation between the polar *R*3 phase ($\lambda = 1$) and the centrosymmetric phase ($\lambda = 0$). As shown in Fig. 6(a), the structural distortion energy curves of *R*3-Zn_3TeO_6 under all strain conditions exhibit a double-well potential, indicating robust ferroelectricity. The ferroelectric well depths are 0.86 eV (unstrained), 1.52 eV (compressive strain), and 0.53 eV (tensile strain). Because the calculations correspond to three formula units, the averaged well depths per Zn_3TeO_6 formula unit are 0.29 eV, 0.51 eV, and 0.18 eV, respectively. Under compressive strain, the well depth (0.51 eV $f.u^{-1}$) becomes comparable to that of the classical ferroelectric $BiFeO_3$ (0.43 eV $f.u^{-1}$),[40] demonstrating that compressive strain enhances the stability of the ferroelectric phase. The calculated spontaneous polarization of *R*3-Zn_3TeO_6

Open Access Article. Published on 02 January 2026. Downloaded on 2/10/2026 6:34:07 PM.
This article is licensed under a Creative Commons Attribution-NonCommercial 3.0 Unported Licence.

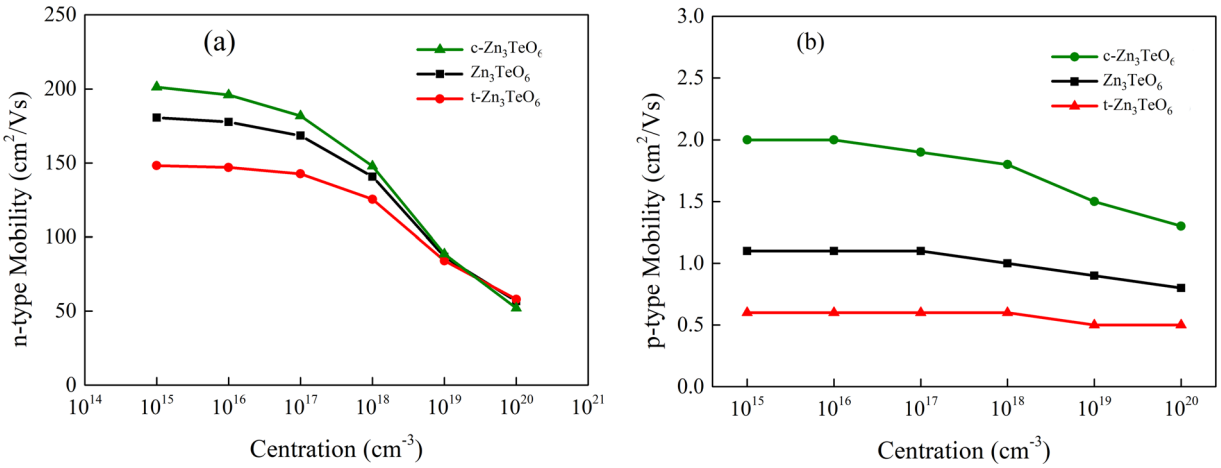

Fig. 7 The (a) electron and (b) hole mobility as a function of concentration for semiconductor Zn_3TeO_6 by AMSET code.

increases from 59.07 μC cm^{-2} (unstrained) to 63.00 μC cm^{-2} under compressive strain, approaching the reported value of 72 μC cm^{-2} for Ni_3TeO_6.[9] This enhancement originates from the reduced interatomic distances and strengthened polar phonon instability induced by compressive strain. Under 3% tensile strain, the polarization decreases to 55.90 μC cm^{-2}, which is consistent with the behavior observed in *R3c*-$BiFeO_3$.[41] Fig. 6(b–d) show that at the polarization endpoints ($\lambda = \pm 1$), compressive strain significantly increases the slope of the polarization curve, indicating a stronger and faster lattice-distortion-induced polarization response. In contrast, tensile strain reduces both polarization and potential-well depth, thereby weakening ferroelectric stability. As shown in Fig. S4, the potential-energy curves under 0%, ±3%, and ±6% strain confirm these trends. Tensile strain gradually shallows the double-well potential and reduces the energy difference between the ferroelectric and paraelectric phases. At 6% tensile strain, the two wells nearly merge, and the interpolation-based Berry-phase method fails to converge. Conversely, 6% compressive strain deepens the ferroelectric–paraelectric potential well and increases the spontaneous polarization to 67.94 μC cm^{-2}.

3.4 Mobility

The carrier mobility of semiconductors governs the electrical conductivity and switching performance of devices and is therefore critical for many applications. Fig. 7 presents the electron and hole mobilities of the three structures as a function of n-type and p-type carrier concentrations, calculated using the AMSET code within the momentum relaxation time approximation (MRTA) framework.[42] In these calculations, four dominant scattering mechanisms are explicitly considered: acoustic deformation potential (ADP) scattering, piezoelectric (PIE) scattering, polar optical phonon (POP) scattering, and ionized impurity (IMP) scattering. The total mobility is obtained by combining the contributions from these scattering processes, and all relevant parameters are derived from first-principles calculations. For ADP scattering, small uniaxial (or isotropic) strains are applied to the crystal, and the band structures are recalculated for each strain value. The deformation potential constant E_1 is then obtained by linearly fitting the variation of the conduction-band minimum (CBM) or valence-band maximum (VBM) energy with respect to strain, as summarized in Table 5, while the corresponding elastic constants are taken from Table 2. For PIE scattering, the piezoelectric tensor is evaluated using density functional perturbation theory (DFPT) under small strains by computing the change in polarization and is subsequently combined with the elastic constants and piezoelectric tensor for transport calculations Tables 2 and 6. For POP scattering, the longitudinal optical (LO) phonon frequency at the Γ point, together with the static and high-frequency dielectric constants (ε_0 and ε_∞), is obtained from

Table 5 The calculated the deformation potential calculations (eV)

		VBM			CBM		
		D_{XX}	D_{YY}	D_{ZZ}	D_{XX}	D_{YY}	D_{ZZ}
c-Zn_3TeO_6 (−3%)	D_{XX}	0.20	0.92	0.11	5.56	0.18	0.03
	D_{YY}	0.92	0.22	0.03	0.18	5.57	0.08
	D_{ZZ}	0.11	0.03	2.32	0.03	0.08	7.87
Zn_3TeO_6	D_{XX}	0.72	0.56	0.22	5.64	0.05	0.12
	D_{YY}	0.56	0.71	0.21	0.05	5.64	0.11
	D_{ZZ}	0.22	0.21	1.83	0.12	0.11	5.83
t-Zn_3TeO_6 (3%)	D_{XX}	1.61	0.22	0.31	5.67	0.09	0.1
	D_{YY}	0.22	1.62	0.32	0.09	5.66	0.1
	D_{ZZ}	0.31	0.32	0.95	0.1	0.1	4.16

Table 6 The calculated piezoelectric tensor (C/m^{-2})

		XX	*YY*	*ZZ*	*XY*	*YZ*	*ZX*
c-Zn_3TeO_6	*X*	0.30	−0.30	0.00	0.12	0.00	−0.06
	Y	0.12	−0.12	0.00	−0.30	−0.06	0.00
	Z	−0.08	−0.08	−0.63	−0.01	0.00	0.00
Zn_3TeO_6	*X*	0.34	−0.34	0.00	0.25	0.05	−0.07
	Y	0.25	−0.25	0.00	−0.34	−0.06	−0.05
	Z	−0.56	−0.56	−1.10	−0.01	0.00	0.00
t-Zn_3TeO_6	*X*	0.45	−0.45	0.00	0.37	0.05	−0.15
	Y	0.37	−0.37	0.00	−0.45	−0.14	−0.05
	Z	−0.66	−0.66	−1.47	0.00	0.00	0.00

© 2026 The Author(s). Published by the Royal Society of Chemistry

Open Access Article. Published on 02 January 2026. Downloaded on 2/10/2026 6:34:07 PM. This article is licensed under a Creative Commons Attribution-NonCommercial 3.0 Unported Licence.

Table 7 Parameters and results of mobility calculation. ω_0 is polar-optical phonon frequency (THz), ε_0 and ε_∞ are static dielectric constant and high-frequency dielectric constant and m^* is effective mass (m_e). S is the scattering rate of the material at a doping concentration of 10^{-18} cm^{-3} (10^{12} S^{-1})

						S			
		ω_0	ε_0	ε_∞	m^*	ADP	IMP	PIE	POP
c-Zn_3TeO_6	Electron	10.82	14.82	4.72	0.23	6.6	13.9	19.5	252
	Hole				6.88	6.6	12.7	19.5	252
Zn_3TeO_6	Electron	10.04	17.3	4.85	0.21	9.1	15.9	58.5	271
	Hole				8.01	9.1	14.4	58.5	271
t-Zn_3TeO_6	Electron	9.23	21.09	5.09	0.18	20.8	14.4	195	295
	Hole				8.46	20.8	12.9	195	295

DFPT Table 7, and these quantities are used to construct a Fröhlich-type electron–LO phonon coupling model. For IMP scattering, all dopants are assumed to be fully ionized, and the ionized impurity concentration is set equal to the carrier concentration specified in the transport calculations. The impurity charge number Z is chosen according to the assumed dopant valence, while the dielectric constant obtained from first-principles calculations is used to describe the screening of the coulomb interaction.

Within AMSET, the carrier mobility at different n-type and p-type doping levels is computed consistently under the MRTA framework. In this approach, doping is not modeled by explicit atomic substitution; instead, the target carrier concentration is provided as an input parameter. For a given electron or hole concentration, AMSET self-consistently determines the corresponding Fermi level and evaluates the scattering rates arising from ADP, POP, IMP, and other relevant mechanisms, and then solves the Boltzmann transport equation to obtain mobility. In this way, the dependence of electron and hole mobilities on n-type and p-type carrier concentrations is systematically established without modifying the underlying crystal structure.

The results show that at a moderate doping concentration of 10^{18} cm^{-3}, the electron mobility for all three structures exceeds 150 cm^2 V^{-1} s^{-1}, approaching that of conventional semiconductor ZnO.[43] The hole mobility is two orders of magnitude lower than the electron mobility, indicating that Zn_3TeO_6 is characterized by strong n-type behavior. From the input parameters Table 7, the hole effective mass is significantly larger than the electron effective mass, consistent with the relatively flat band structure near the VBM. This results in substantially lower hole transport capability compared to electrons. Among the scattering mechanisms, POP scattering dominates, reaching an order of magnitude of approximately 10^{14} s^{-1}, which critically determines the carrier relaxation time.

Notably, among the three structures c-Zn_3TeO_6 exhibits the highest electron mobility value. Although compressive strain slightly increases the effective mass of Zn_3TeO_6, it concurrently elevates the characteristic frequency ω_0 of the polar optical phonons. As evident in the phonon dispersion spectra Fig. 3, c-Zn_3TeO_6 possesses higher optical phonon frequencies. A higher ω_0 implies that greater energy is required for electrons to exchange energy with optical phonons, thereby significantly reducing POP scattering intensity. Furthermore, as strain transitions from tensile to compressive, the high-frequency dielectric constant ε_∞ and the static dielectric constant ε_0 decrease slightly. Since the polar coupling strength is proportional to $\frac{1}{\varepsilon_\infty} - \frac{1}{\varepsilon_0}$, which equals 0.149, 0.148, and 0.144 for the t-Zn_3TeO_6, Zn_3TeO_6, and c-Zn_3TeO_6 structures respectively, compressive strain weakens polar coupling, further suppressing POP scattering. For PIE scattering, under tensile strain, the scattering rate can reach the order of 10^{14} s^{-1}, highlighting its significant contribution to carrier scattering. However, as shown in Table 6, under compressive strain, the tensor components of the piezoelectric coefficients are notably reduced due to decreased lattice dimensions and restricted atomic displacements. This reduction stems from the smaller lattice dimensions and constrained atomic displacements within the unit cell, leading to diminished piezoelectric response and consequently reduced PIE scattering intensity. Overall, the analysis shows that compressive strain helps suppress the dominant scattering mechanisms POP and PIE, thereby enhancing the electron mobility in Zn_3TeO_6.

4. Conclusion

Using density functional theory, the elastic constants, phonon spectra, and molecular dynamics of $R3$-Zn_3TeO_6 under compressive and tensile strain were systematically investigated to assess its structural stability. Electronic structure analyses reveal that the valence band is predominantly determined by Zn–O interactions, while the conduction band mainly arises from Te–O hybridization. Under compressive strain, the O orbital contribution near the valence band maximum decreases and the conduction band minimum shifts upward, resulting in a bandgap widening from 2.60 eV to 2.72 eV. Conversely, tensile strain enhances the O orbital contribution and lowers the conduction band minimum, narrowing the bandgap to 2.36 eV—favorable for visible-light absorption. Compressive strain significantly enhances the ferroelectric polarization of Zn_3TeO_6, conferring excellent ferroelectric performance and structural robustness. In terms of charge transport, Zn_3TeO_6 exhibits high electron mobility (>150 cm^2 V^{-1} s^{-1}) and hole mobility two orders of magnitude lower, indicative of a strong n-type character. Notably, compressive strain further promotes electron mobility through increased optical phonon frequencies and reduced piezoelectric coefficients, effectively suppressing carrier scattering. These results provide theoretical insight into the potential of $R3$-Zn_3TeO_6 for stable, high-performance ferroelectric and optoelectronic applications.

Conflicts of interest

The authors declared that they have no conflicts of interest to this work. We declare that we do not have any commercial or associative interest that represents a conflict of interest in connection with the work submitted.

Open Access Article. Published on 02 January 2026. Downloaded on 2/10/2026 6:34:07 PM. This article is licensed under a Creative Commons Attribution-NonCommercial 3.0 Unported Licence.

Data availability

The data that support the findings of this study are available from the corresponding author upon reasonable request.

Supplementary information (SI) is available. See DOI: https://doi.org/10.1039/d5ra08570e.

Acknowledgements

This work was supported by the Maoming Municipal Science and Technology Program (No 2023023), the Guangdong University of Petrochemical Technology 2022 University-level Educational and Teaching Reform Research Project (No. JY202245), Guangdong Provincial Key Areas Special Project for Regular Higher Education Institutions (Grant No. 2023ZDZX3014).

References

1 M. Hudl, R. Mathieu, S. A. Ivanov, *et al.*, Complex magnetism and magnetic-field-driven electrical polarization of Co_3TeO_6, *Phys. Rev. B:Condens. Matter Mater. Phys.*, 2011, **84**, 180404.
2 S. A. Ivanov, R. Tellgren, C. Ritter, *et al.*, Temperature-dependent multi-k magnetic structure in multiferroic Co_3TeO_6, *Mater. Res. Bull.*, 2012, **47**, 63–72.
3 J. W. Kim, S. Artyukhin, E. D. Mun, *et al.*, Successive magnetic-field-induced transitions and colossal magnetoelectric effect in Ni_3TeO_6, *Phys. Rev. Lett.*, 2015, **115**, 137201.
4 X. Zhu, Z. Wang, X. Su, *et al.*, New Cu_3TeO_6 ceramics: phase formation and dielectric properties, *ACS Appl. Mater. Interfaces*, 2014, **6**, 11326–11332.
5 S. A. Ivanov, P. Nordblad, R. Mathieu, *et al.*, New type of incommensurate magnetic ordering in Mn_3TeO_6, *Mater. Res. Bull.*, 2011, **46**, 1870–1877.
6 M. Weil, Zn_3TeO_6, *Struct. Rep.*, 2006, **62**, i246–i247.
7 W. Massa, Die Kristallstruktur von β-Li_3VF_6, *Z. Kristallogr.–Cryst. Mater.*, 1980, **153**, 201–210.
8 R. Becker, M. Johnsson and H. Berger, A new synthetic cobalt tellurate: Co_3TeO_6, *Cryst. Struct. Commun.*, 2006, **62**, i67–i69.
9 Y. Han, M. Wu, C. Gui, *et al.*, Data-driven computational prediction and experimental realization of exotic perovskite-related polar magnets, *NPJ Quantum Mater.*, 2020, **5**, 92.
10 K. Fujiwara, *et al.*, Thin-film stabilization of $LiNbO_3$-type $ZnSnO_3$ and $MgSnO_3$ by molecular-beam epitaxy, *APL Mater.*, 2019, **7**, 022505.
11 X. Han, *et al.*, $MgSnO_3$ epitaxial thin films for solar-blind photodetection: Fabrication and properties, *Vacuum*, 2024, **226**, 113340.
12 J. Fernández-Catalá, H. Singh, S. Wang, *et al.*, Hydrothermal synthesis of Ni_3TeO_6 and Cu_3TeO_6 nanostructures for magnetic and photoconductivity applications, *ACS Appl. Nano Mater.*, 2023, **6**, 4887–4897.
13 E. Selb, L. Declara, L. Bayarjargal, *et al.*, Crystal Structure and Properties of a UV-Transparent High-Pressure Polymorph of Mg_3TeO_6 with Second Harmonic Generation Response, *Eur. J. Inorg. Chem.*, 2019, 4668–4676.
14 D. Reichartzeder, M. Wildner, M. Weil, *et al.*, Crystal Chemistry, Optical Spectroscopy and Crystal Field Calculations of Co_3TeO_6 and Solid Solutions Co_3–$xZnxTeO_6$, *Eur. J. Inorg. Chem.*, 2018, 4221–4233.
15 T. Sarkar, S. A. Ivanov, M. Weil, *et al.*, Compositional dependence of the magnetic state of Co_3- $xZnxTeO_6$ solid solutions, *J. Alloys Compd.*, 2021, **884**, 161111.
16 G. Song and W. Zhang, Comparative studies on the room-temperature ferrielectric and ferrimagnetic Ni_3TeO_6-type A_2FeMoO_6 compounds (A = Sc, Lu), *Sci. Rep.*, 2016, **6**, 20133.
17 A. F. Lima, Electronic and optical properties of the R3 Ni_3TeO_6 compound described by the modified Becke-Johnson exchange potential, *Opt. Mater.*, 2023, **136**, 113419.
18 M. Ye and D. Vanderbilt, Ferroelectricity in corundum derivatives, *Phys. Rev. B*, 2016, **93**, 134303.
19 H. Shu and J. Guo, Enhanced stability and tunable optoelectronic properties of silicon–carbon monolayers by strain and surface functionalization, *J. Mater. Chem. C*, 2024, **12**(16), 5916–5925.
20 H. Shu, Assessing stability and optoelectronic properties of 2D carbon-boron compounds under elastic strains, *Surf. Interfaces*, 2025, 106702.
21 H. Shu and H. Xu, Effects of strain on the stability, electronic, and optical properties of new h-BC 2 N: a many-body study, *Phys. Chem. Chem. Phys.*, 2025, **27**(32), 16972–16979.
22 D. G. Schlom, L. Q. Chen, X. Pan, *et al.*, A thin film approach to engineering functionality into oxides, *J. Am. Ceram. Soc.*, 2008, **91**, 2429–2454.
23 J. Li, Y. Lee, Y. Choi, *et al.*, The classical-to-quantum crossover in the strain-induced ferroelectric transition in $SrTiO_3$ membranes, *Nat. Commun.*, 2025, **16**, 4445.
24 Y. Hu, J. Yang and S. Liu, Giant piezoelectric effects of topological structures in stretched ferroelectric membranes, *Phys. Rev. Lett.*, 2024, **133**, 046802.
25 H. L. Liu, M. K. Lin, Y. R. Cai, *et al.*, Strain modulated optical properties in $BiFeO_3$ thin films, *Appl. Phys. Lett.*, 2013, **103**, 181907.
26 M. Sharma, *et al.*, Lattice strain engineering in Ni_3TeO_6 nanostructure for enhanced oxygen evolution reaction in alkaline medium, *Int. J. Hydrogen Energy*, 2025, **132**, 116–129.
27 D. Sando, Y. Yang, C. Paillard, *et al.*, Epitaxial ferroelectric oxide thin films for optical applications, *Appl. Phys. Rev.*, 2018, **5**, 041108.
28 G. Kresse and J. Furthmüller, Efficient iterative schemes for ab initio total-energy calculations using a plane-wave basis set, *Phys. Rev. B:Condens. Matter Mater. Phys.*, 1996, **54**, 11169–11186.
29 G. Kresse and J. Hafner, Ab initio molecular dynamics for open-shell transition metals, *Phys. Rev. B*, 1993, **48**, 13115–13118.
30 G. Kresse and D. Joubert, From ultrasoft pseudopotentials to the projector augmented-wave method, *Phys. Rev. B*, 1999, **59**, 1758–1775.

© 2026 The Author(s). Published by the Royal Society of Chemistry

Open Access Article. Published on 02 January 2026. Downloaded on 2/10/2026 6:34:07 PM.
This article is licensed under a Creative Commons Attribution-NonCommercial 3.0 Unported Licence.

31 J. P. Perdew, K. Burke and M. Ernzerhof, Generalized gradient approximation made simple, *Phys. Rev. Lett.*, 1996, **77**, 3865–3868.
32 J. Heyd, G. E. Scuseria and M. Ernzerhof, Hybrid functionals based on a screened Coulomb potential, *J. Chem. Phys.*, 2003, **118**, 8207–8215.
33 O. A. Vydrov and G. E. Scuseria, Assessment of a long-range corrected hybrid functional, *J. Chem. Phys.*, 2006, **125**, 234109.
34 A. Togo, First-principles phonon calculations with phonopy and phono3py, *J. Phys. Soc. Jpn.*, 2023, **92**, 012001.
35 F. Mouhat and F. X. Coudert, Necessary and sufficient elastic stability conditions in various crystal systems, *Phys. Rev. B*, 2014, **90**, 224104.
36 X. F. Xu, X. L. Cai, K. R. Su, *et al.*, Tuning mechanical properties, ferroelectric properties and electronic structure in R3c-$MgSnO_3$ by compressive strain: A first-principle study, *Phys. B*, 2021, **618**, 413143.
37 R. Hill, The elastic behaviour of a crystalline aggregate, *Proc. Phys. Soc. A.*, 1952, **65**(5), 349.
38 R. Resta, Macroscopic polarization in crystalline dielectrics: the geometric phase approach, *Rev. Mod. Phys.*, 1994, **66**, 899–915.
39 R. D. King-Smith and D. Vanderbilt, Theory of polarization of crystalline solids, *Phys. Rev. B*, 1993, **47**, 1651–1654.
40 S. Song, H. M. Jang, N. S. Lee, *et al.*, Ferroelectric polarization switching with a remarkably high activation energy in orthorhombic $GaFeO_3$ thin films, *NPG Asia Mater.*, 2016, **8**, e242.
41 C. Ederer and N. A. Spaldin, Effect of epitaxial strain on the spontaneous polarization of thin film ferroelectrics, *Phys. Rev. Lett.*, 2005, **95**, 257601.
42 A. M. Ganose, J. Park, A. Faghaninia, *et al.*, Efficient calculation of carrier scattering rates from first principles, *Nat. Commun.*, 2021, **12**, 2222.
43 E. M. Likovich, K. J. Russell, E. W. Petersen, *et al.*, Weak localization and mobility in ZnO nanostructures, *Phys. Rev. B: Condens. Matter Mater. Phys.*, 2009, **80**, 245318.